Materials & Design 234 (2023) 112308

Contents lists available at ScienceDirect

Materials & Design

journal homepage: www.elsevier.com/locate/matdes

Multi-instrumental approach to domain walls and their movement in ferromagnetic steels – Origin of Barkhausen noise studied by microscopy techniques

Suvi Santa-aho [a,*], Mari Honkanen [b], Sami Kaappa [c], Lucio Azzari [b], Andrey Saren [d], Kari Ullakko [d], Lasse Laurson [c], Minnamari Vippola [a,b]

[a] Materials Science and Environmental Engineering, Faculty of Engineering and Natural Sciences, Tampere University, P.O. Box 589, 33104 Tampere University, Finland
[b] Tampere Microscopy Center, Tampere University, P.O. Box 692, 33014 Tampere University, Finland
[c] Computational Physics Laboratory, Faculty of Engineering and Natural Sciences, Tampere University, P. O. Box 692, 33104 Tampere University, Finland
[d] Material Physics Laboratory, Lappeenranta-Lahti University of Technology LUT, P.O. Box 20, 53851 LUT University, Finland

ARTICLE INFO

Keywords:
Ferromagnetic steel
Magnetic domains
Domain wall dynamics
Barkhausen noise
Magnetic force microscopy
Lorentz microscopy

ABSTRACT

Two steels, ferrite and ferrite-pearlite were thoroughly characterized by a multi-instrumental microscopy techniques to get detailed information about their microstructure and magnetic structure. Microstructural features act as pinning sites for the motion of magnetic domain walls (DWs) leading to changes in the magnetization of the sample. This phenomenon is the basis for industrially relevant non-destructive Barkhausen noise (BN) technique. With magnetic force microscopy (MFM), using bulk samples, and Lorentz microscopy, using thin films, we noticed that bulk and thin samples have similar domain structure still giving different BN signal amplitudes. We could explain an in-plane DW movement under out-of-plane applied magnetic field using anisotropy energetics. *In-situ* transmission electron microscopy (TEM) in Lorentz mode was used to visualize the motion of DWs and their interactions with different pinning sites. To help the interpretation of DW motions, alignment and denoising processes were tailored for *in-situ* TEM studies. Multi-instrumental and multidimensional structural analysis enabled us to visualize and verify many theoretical hypotheses related to the origin of BN signal in ferrite and ferrite-pearlite steels.

1. Introduction

Magnetic Barkhausen noise (BN) is generated by the motion of magnetic domain walls (DWs) in the ferromagnetic material, exposed to a time-varying external magnetic field. DWs are boundaries separating different magnetic regions having varying internal magnetization directions. DW movements are hindered by pinning sites including, for example, grain boundaries, dislocations, and precipitates, leading to discontinuous and abrupt changes in the magnetization of the workpiece as the DWs respond to the slowly changing external magnetic field by exhibiting a sequence of irregular jumps of propagation. These abrupt changes can be measured with an inductive coil, resulting in an induced bursty voltage signal known as the Barkhausen noise. Non-destructive BN method is widely utilized in industrial quality control processes after manufacturing processes such as grinding to detect localized microstructure and stress variations. However, all the hypotheses, related to the domain structure and DW movement, have not been scientifically verified, and the BN method applicability is still limited because of controversial results due to the stochastic nature of the phenomenon itself [1]. Combining different micro- and nano-scale characterization techniques has great potential in understanding the BN measurement outcome better and to connect Barkhausen noise to the DWs and their interactions with microstructural details.

Currently, most of the studies of domains are limited to visualizing them in 2D samples by magneto-optical Kerr effect (MOKE) [2], magnetic force microscopy (MFM) or transmission electron microscopy (TEM) [3], for example. The imaging of thin magnetic films in TEM is based on the special mode called Lorentz microscopy [4]. In the technique, the Lorentz lens is used for imaging while the normal objective lens (OL) is turned off. The contrast of DWs in the images is created

* Corresponding author.
E-mail addresses: suvi.santa-aho@tuni.fi (S. Santa-aho), mari.honkanen@tuni.fi (M. Honkanen), sami.kaappa@tuni.fi (S. Kaappa), lucio.azzari@tuni.fi (L. Azzari), andrey.saren@lut.fi (A. Saren), kari.ullakko@lut.fi (K. Ullakko), lasse.laurson@tuni.fi (L. Laurson), minnamari.vippola@tuni.fi (M. Vippola).

https://doi.org/10.1016/j.matdes.2023.112308
Received 16 June 2023; Received in revised form 18 August 2023; Accepted 5 September 2023
Available online 7 September 2023

while the Lorentz force deflects the electrons passing by the sample. However, only magnetic domains that are oriented in a specific perpendicular direction compared to the passing electrons will produce deflection enough to be imaged [5]. MFM is an atomic force microscopy (AFM)-based technique, with which the topography and magnetic properties of bulk samples can be simultaneously visualized [5]. In MFM, the cantilever is deflected by the magnetic interaction force between the magnetic tip and sample surface stray fields. This phase shift gives the contrast of images and is proportional to the magnetic force gradient in vertical direction. Sections with strong stray field normal to the studied surface give the best contrast. Contrast formation depends on the orientation of the grains as well [6]. The influence of external magnetic field can also be studied while imaging the sample with MFM [6,7]. Abuthinar and Kumar [7] used MFM to study the effects of crystallographic orientation and external magnetic field in polycrystalline iron. Batista *et al.* [6] used MFM together with TEM to reveal the specific microstructural details, such as dislocations, affecting the DWs in high purity iron and two unalloyed steels, Fe-0.8 %C and Fe-1.5 %C, containing Fe_3C carbides in the ferrite matrix. They studied the sample first with MFM where the images showed branched magnetic structure that was explained by accumulation of dislocations. This was verified by TEM showing that dislocations nucleate at the edge of the interface between cementite and ferrite. Thus, usually the domains are represented in 2D plane even if the real structures are in 3D. This is because of the lack of appropriate experimental 3D methods. Manke *et al.* [3,8] used Talbot-Lau neutron tomography technique for direct imaging of the 3D domains. Di Pietro Martinez *et al.* [9] utilized a novel technique called Fourier transform holography for 3D imaging of domains in the 800-nm-thick Fe/Gd multilayer sample on the Si_3N_4 membrane. They noticed that domains were wormlike with magnetization pointing mostly out of plane near the surface of the sample but falling in-plane near the substrate. 3D techniques have also drawbacks, e.g., very long measurement times [8] and limited resolutions [8,9] and thus the technique might be combined with other imaging methods such as electron microscopy [3].

Besides the utilization of many microscopy methods, different *in-situ* characterization methods have been used in the studies of magnetic domain structures. Kim and Park [10] utilized *in-situ* Lorentz microscopy when studying changes in the magnetic domain structure during heating. They visualized the temperature-dependent dynamics of magnetic domains of Z-type hexagonal ferrite with videos. They used the transport of intensity equation (TIE) technique to reconstruct the magnetic domains and reveal the magnetization vector directions in TEM images. Ickler *et al.* [11] utilized scanning electron microscopy (SEM) together with electron backscatter diffraction (EBSD) method for magnetic domain studies during *in-situ* deformation experiment with tensile modulus. The imaging of magnetic domains was carried out with a forescatter electron detector in SEM-EBSD.

In this study, two microstructures of steel, ferrite and ferrite-pearlite, were thoroughly characterized by various microscopy methods. Combination of information gathered by SEM-EBSD, SEM-transmission Kikuchi diffraction (TKD), TEM-Lorentz microscopy, and MFM was used to get fundamental information about microstructural features, i.e., pinning sites of the DW motion and their interaction with DWs. These findings were utilized to make the connection between microstructural features and BN output, i.e., to explain the origin of the BN signal. SEM-TKD and Lorentz microscopy require a very thin sample (<100 nm). However, in industrial applications, BN measurements are carried out for bulk samples. Thus, here we utilized MFM using bulk samples to compare and combine results of thin and bulk samples. This comparison was very important because we used *in-situ* TEM studies on thin samples to visualize the motion of DWs and we connected these findings to BN signals measured from the bulk samples. Even though our research group has been studying Barkhausen noise since 2007 (e.g. [12–14]), this was the first time to really apply comprehensive microscopy methods. In our recent study [15], we used *in-situ* TEM to visualize and mimic a BN measurement of martensitic and ferrite-pearlitic steels. Here, we concentrated on the effects of different, individual pinning sites on the DW motion and how they are connected to the BN output. Inspected samples were plain ferrite with simple microstructure and magnetic structure and industrially relevant ferrite-pearlite with more complex structures. Pearlitic steels are commonly used in automotive plate steel components [16]. Typically, destructive laboratory methods, e.g., SEM imaging, have been utilized for determining the pearlite content. The replacement of destructive methods to non-destructive testing (NDT) methods is highly tempting for time and money savings. In addition, Altpeter [17] pointed out the need to nondestructively inspect the cementite (Fe_3C) content by magnetic techniques as the volume fraction and morphology contributes to the yield strength of steels.

2. Materials and methods

2.1. Material

Two commercial hot-rolled steels with different microstructures were studied: ferrite and ferrite-pearlite. Compositions of steels (Table 1) were determined in Metlab Oy (Finland) by optical emission spectroscopy (OES).

2.2. Characterization of microstructure

Microstructures of ferrite and ferrite-pearlite samples were studied with SEM (Ultraplus, Carl Zeiss AG, Germany) together with an EBSD system (Symmetry, Oxford Instruments, UK), and by TEM (JEM-F200, JEOL, Japan). Forescatter diodes (FSD) in the EBSD system generating images with topography and orientation contrast were used for microstructural imaging. To get crystallographic information, EBSD was used and to improve a spatial resolution of EBSD, TKD method was utilized. SEM-EBSD samples, i.e., bulk samples, were prepared from ferritic and ferritic-pearlitic materials with a traditional metallographic method. Small sections (ferrite: 10 mm × 22 mm, ferrite-pearlite: 9 mm × 20 mm) were cut from the steel plates and hot-mounted into resin (Polyfast, Struers, Denmark). After the mounting, the samples were ground by 320 – 2000 SiC papers and polished with 3 μm and 1 μm diamond suspensions followed by polishing with colloidal silica suspension. The final polishing for EBSD samples was done with a cooling cross section polisher (IB-19520CCP, JEOL, Japan). SEM samples were used to study microstructures also with an optical microscope (OM, ECLIPSE MA100, Nikon, Japan). Prior to OM studies, the samples were etched by 4 % Nital (nitric acid in methanol). SEM-EBSD samples were prepared in both top view and cross-section directions (Fig. 1a). SEM-TKD and TEM samples, i.e., thin samples, were prepared from the top view direction (Fig. 1b). They were prepared by machining 3 mm diameter discs (thickness < 100 μm) and then by electropolishing (TenuPol, Struers, Denmark) the discs until perforation using a solution (-25 °C) of nitric acid in methanol (1:3). If needed, TKD + TEM samples were further thinned by a precision ion polishing system (Model 691, Gatan, USA).

In the EBSD and TKD measurements, acceleration voltages 20 kV and 30 kV were used, respectively. Step sizes used were selected according to the features studied. The EBSD and TKD data was collected by the Aztec software and post-processed using the AztecCrystal software (both from Oxford Instruments, UK). Grain orientations are presented with EBSD inverse pole figure (IPF) maps together with IPF color key (normal direction, Z0). Phase distribution is shown with EBSD/TKD phase maps. Dislocations that contribute to the bending of the crystal lattice are referred to as geometrically necessary dislocations (GNDs) and these dislocations can be measured by EBSD. Here, advanced dislocation analysis was performed using an approach known as the Weighted Burgers Vector (WBV) technique. A true dislocation density will almost always be higher than a density calculated from 2D EBSD data. However, the WBV approach gives significant knowledge about dislocations

Table 1
Chemical composition of both materials determined in Metlab Oy by OES.

[%]	C	Si	Mn	P	S	Cr	Ni	Mo	Cu	Ti	V	Al	Nb	W	Fe
Ferrite	0.036	0.012	0.186	0.07	0.008	0.037	0.044	0.007	0.041	<0.003	0.004	<0.005	<0.005	<0.02	Bal.
Ferrite-pearlite	0.714	0.273	0.669	0.012	0.006	0.085	0.08	0.019	0.148	<0.003	0.003	0.028	<0.005	<0.02	Bal.

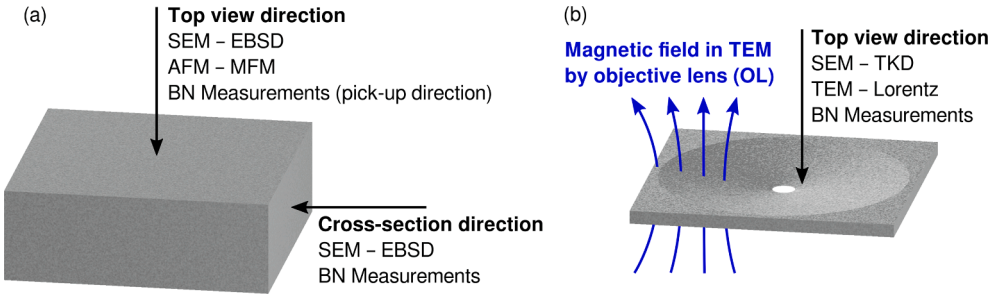

Fig. 1. Measurement directions of (a) bulk sample and (b) thin film.

and the assumptions necessary in other dislocation analysis methods are not needed [18]. In this study, dislocation densities are presented as GND density maps collected by TKD method.

2.3. Characterization of magnetic structure

Domain walls in the *thin* samples were studied by Lorentz microscopy using TEM: Low Mag mode was used, i.e., an objective mini-lens was used for imaging and the normal objective lens (OL) was switched off. This tries to minimize the magnetic field in the sample area. The Fresnel mode, i.e., a defocused condition, was used: underfocused and overfocused images reveal DWs as white or black lines.

Magnetic structure in the *bulk* samples was studied by magnetic force microscopy (MFM) which is atomic force microscopy (AFM) -based technique. In the first step of the MFM measurement, the topography of the sample is measured as in the standard AFM mode. After that, the second scan of the surface is performed at fixed tip-sample distance (lift mode) based on the first scan. Thus, topography and MFM images are consecutively collected from the same sample area. Due to the magnetic coating of the MFM tip and the presence of magnetic samples, the tip experiences a magnetic force on the sample surface. This force produces a variation in the amplitude and a shift in the phase of the oscillation of the cantilever. In MFM, these variations and shifts are recorded, and DWs can be observed as bright and dark lines [6]. The MFM phase shift (angle difference) seen as the contrast variations is mainly proportional to the magnetic force gradient in the vertical direction as described in [6]. This phase angle detection, that is the color key in MFM images, measures the cantilever's phase of oscillation relative to the piezo drive, indicating if these areas are repelling the tip or attracting the tip. The best contrast in MFM is gained with areas that have strong stray field normal to surface, that is parallel to the tip axis. In addition, as described in [7], the contrast depends on the specific orientations of the grains with respect to hard/easy magnetization axes. In this study, two AFM/MFM systems were used: Nanoscope iCon (Bruker, Germany, located at Tampere University, Finland) and XE7 (Park Systems, Korea, located at LUT University, Finland). The tip used in Nanoscope iCon was MESP-LM-V2 and in XE7 was PPP-MFMR. Image post-processing for MFM scans included only basic flattening operations. The MFM scans were performed for the SEM samples in the top view direction (Fig. 1a).

2.4. Visualization of domain wall motion

DW movements were studied with *in-situ* TEM by using the standard OL as a vertical source of the applied magnetic field (the sample was always un-tilted) and the objective mini-lens (Lorentz microscopy) was used for imaging. By controlling the excitation of the OL, the strength of the applied field was varied. DW movements were recorded (5 frames per second) by FastStone Capture software (FastStone Corporation, Canada) and post-processed as a video (described below). Here, the strength of the magnetic field produced by the OL was not determined because we concentrated on the interaction between DWs and pinning sites regardless of the strength of the external field. Thus, videos presented here cannot be compared with each other. There, time frames and the strength of the magnetic field vary. However, in the videos, the strength of the external magnetic field always increases as a function of time.

2.4.1. Sequence processing: Alignment and denoising

Because the standard OL was used as the source of the applied magnetic field, a region of interest (ROI) was shifting during the *in-situ* TEM experiments. Therefore, acquired images needed a post-alignment procedure frame by frame. Furthermore, the exposure time used in these *in-situ* experiments was quite short and denoising was applied for the aligned data.

2.4.1.1. Drift compensation: Frame-by-frame alignment. The shift of the ROI must be occasionally compensated manually by a TEM operator before the sample vanishes completely outside the field of view. By construction, the acquisition plane and the sample's plane are parallel to each other; furthermore, we can assume that the drift is 2D, on the same plane as the sample's plane. Thus, it is reasonable to model the drift as a rigid transformation (i.e., 2D shift) between two consecutive frames. Based on this assumption, the algorithm developed by Eslahi and Foi [19] was used for sparse recovery of misaligned multimodal images to align the data. The algorithm uses a multiscale registration approach in which it first computes a shift vector field using block-wise correlation between the two images to be aligned, and then it estimates a single 9x9 deformation matrix using the vector field; the matrix describes the affine transformation to be applied to the target image to obtain the reference image. Because only a rigid transformation is assumed, 7 of the 9 parameters of the transformation matrix are fixed, while only the two parameters that describe the image shift are estimated. Fig. 2(a,b) shows an example of the alignment of frames acquired by Lorentz microscopy. Fig. 2c shows how the algorithm is capable of correctly aligning the frames even if the average intensity and content between reference and target changes significantly.

2.4.1.2. Denoising. Because all the acquisitions will inevitably be affected by noise, it is always convenient to denoise the data. To optimally denoise a sequence, it is necessary to model the acquisition

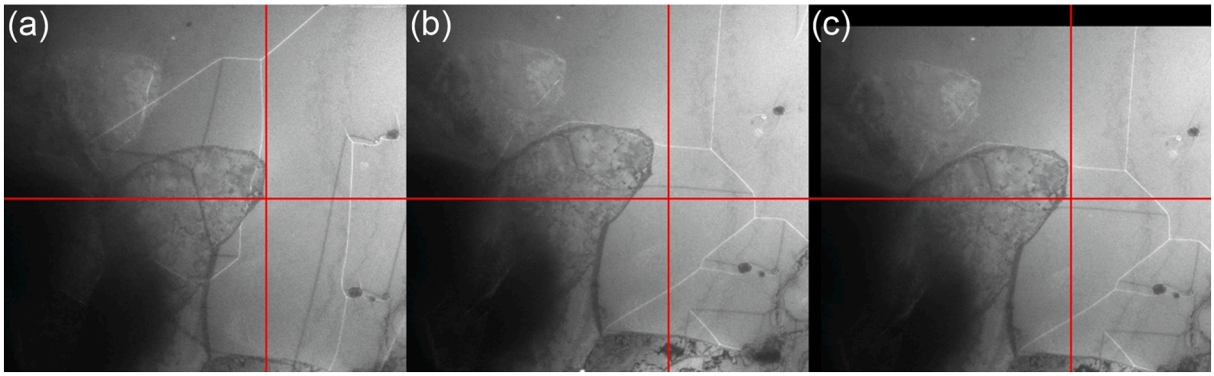

Fig. 2. Example of alignment process, the red cross is at constant position in the sequence, and it is used to visually evaluate the alignment. (a) Reference frame (frame 1) from a ferrite sample sequence acquired using Lorentz microscopy (image width 18 μm), (b) target frame to be aligned (frame 200) from the same sequence, and (c) alignment result. (For interpretation of the references to color in this figure legend, the reader is referred to the web version of this article.)

process: for TEM systems, the observed data z can be assumed to be given by

$$z(x) = y(x) + \eta(x) \tag{1}$$

where y is a deterministic noise-free signal, η is the noise affecting the acquisition, and x is the pixel's coordinate. For a video sequence x is a 3D vector, where the first two elements are the spatial coordinate of the pixel in a frame, while the third coordinate represents the temporal coordinate, that is the frame index. For simplicity, in the reminder of the manuscript we will omit the coordinate x. The observation model in Eq. (1) implies that every acquired frame of a signal is the result of the sum between an underlying noise-free deterministic signal and realizations η of a random process. With denoising we intend to recover y and remove η A complete model for η in the context of Lorentz microscopy acquisitions is the correlated and signal-dependent noise model [20]. Signal-dependent noise implies that the noise strength (e.g., variance) is not constant for each pixel of the acquired data, but it depends on the signal that the noise is affecting. As commonly done in literature [21], it is opportune to model the noise variance as an affine function of the signal expectation:

$$\mathrm{var}[\eta] = \sigma^2(y) = ay + b \tag{2}$$

According to Eq. (2), the variance of the noise affecting a pixel is given by the sum of a component that depends on the pixel's intensity y, and a constant component b. Correlated noise implies that the noise affecting a pixel is correlated with its surroundings through a noise correlation function. This function depends on the covariance matrix of the data's pixels and describes the noise correlation. We model the noise correlation as

$$\eta = \nu * g \tag{3}$$

that is the convolution between a deterministic noise shaping kernel g and a zero-mean white Gaussian random field ν with unitary variance (i.e., $\nu \sim \mathcal{N}(0,1)$). Our signal-dependent correlated noise model is finally expressed as

$$z = y + \sigma(y)\eta \tag{4}$$

Assuming that the ℓ_2 norm of g is unitary, then the variance of z is equal to σ^2, as described in Eq. (2). To denoise the signal-dependent correlated noise, the software developed in Ref. [22] was used. This software, given a noisy input sequence, will at first automatically estimate the parameters of the noise affecting the data, then apply a variance stabilizing transformation (VST) to the data to make the noise signal-independent, and finally optimally denoise the data using a filter for the 3D signals [23].

2.5. Barkhausen noise measurements

Barkhausen noise measurements were carried out with a BN analyzer (Rollscan 350, Stresstech Oy, Finland). A commercial small, curved sensor (S1-11–22-09, S6672) to fit the sample surface (magnetizing unit width totally 5 mm, pick-up unit width 2 mm) was used with 1.5 V peak-to-peak voltage (vpp) and the measurement frequency of 300 Hz for both ferrite and ferrite-pearlite samples. The measurement voltage parameter was selected according to Ref. [24] from the knee region of the voltage sweep suitable for both materials before saturation. The BN measurements were carried out for both the bulk SEM samples (top view and cross-section directions, Fig. 1a) and the pre-thinned sheets for TEM sample preparation (top view direction, Fig. 1b). In the case of the top view direction of the bulk ferrite sample (Fig. 1a), the BN measurements were carried out by applying the driving field in two different directions: the rolling direction (RD) and transverse to the rolling direction (TD). In the case of the pre-thinned samples, thicknesses of the ferrite samples were 0.10 mm and 0.07 mm, and thicknesses of the ferrite-pearlite samples were 0.11 mm and 0.06 mm. All BN measurements were performed with the same measurement parameters. Direct results from the Microscan software were utilized in the analyses. The BN pick-up measurement direction is normal to the surface [25].

3. Results and discussion

3.1. Microstructure of ferrite and ferrite-pearlite

To study the pinning sites affecting DW motions, the microstructures of the ferrite and ferrite-pearlite samples were studied comprehensively by SEM-EBSD, SEM-TKD, and TEM (Fig. 3–5). Based on the FSD image and EBSD data (Fig. 3a), the ferrite sample in the top view direction has slightly elongated grains and they favor [1 1 1] direction in the normal direction (Z0). The ferrite sample in the cross-section direction has slightly flattened grains (Fig. 3b). Ferrite contains cementite (Fe_3C) carbides located both at the grain boundaries and inside the grains (Fig. 4a,b). Small carbides (<500 nm) inside the grains were challenging to index in the bulk sample by EBSD but TKD studies with thin samples indicated them also to be Fe_3C (Fig. 4b). The dislocation density varies spatially (Fig. 4c).

Ferrite-pearlite contains both globular and lamellar Fe_3C carbides in the ferrite matrix (Fig. 5–6). Based on the EBSD studies, the ferrite grains in the pearlite sample are randomly oriented in both top view (Fig. 5a) and cross-section (Fig. 5b) directions. The dislocation density varies spatially (Fig. 6c).

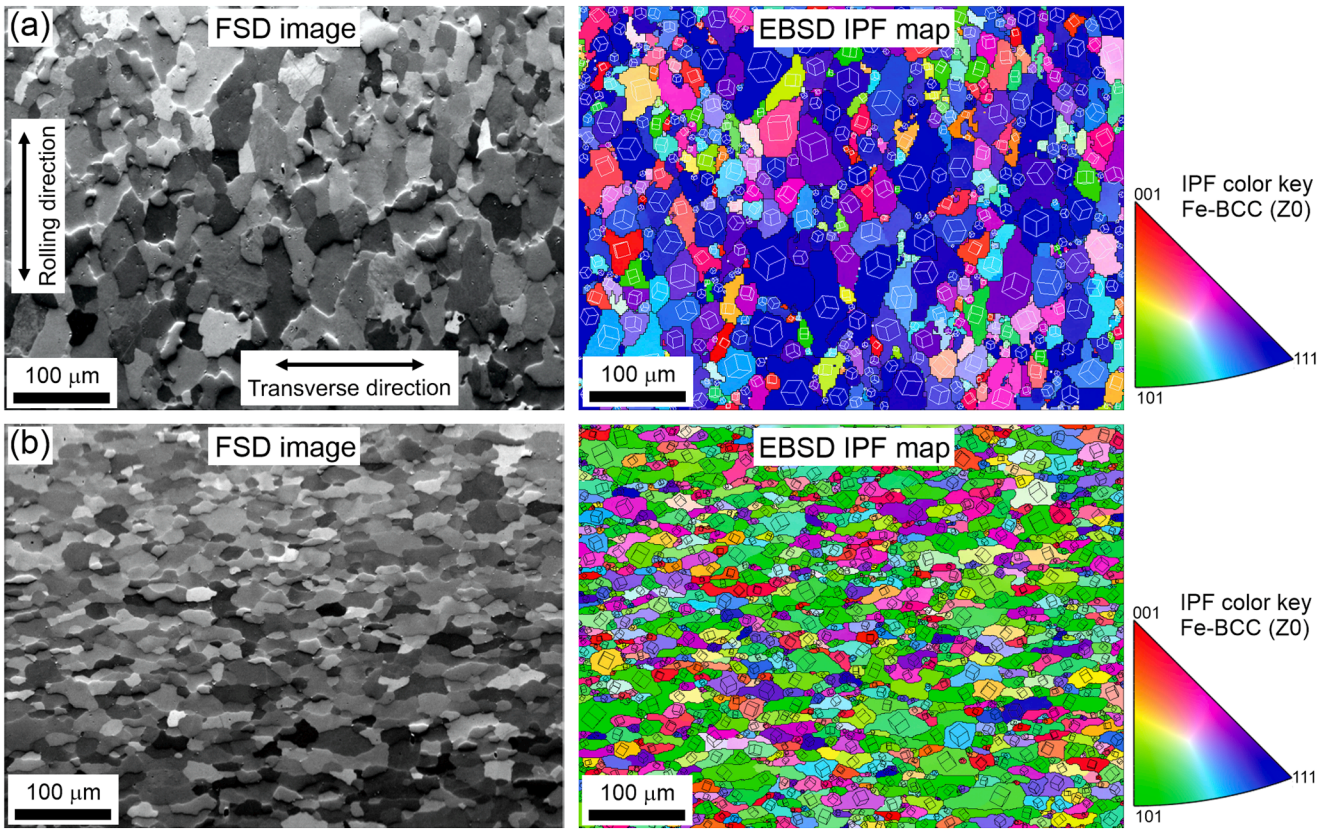

Fig. 3. Microstructure of the ferrite sample: FSD image showing ferrite grains and EBSD IPF map to the normal direction (Z0) with grain boundaries (>10°) and unit cells showing orientations of ferrite grains. (a) Top view direction showing slightly elongated grains favoring the [1 1 1] direction and (b) cross-section direction showing slightly flattened grains.

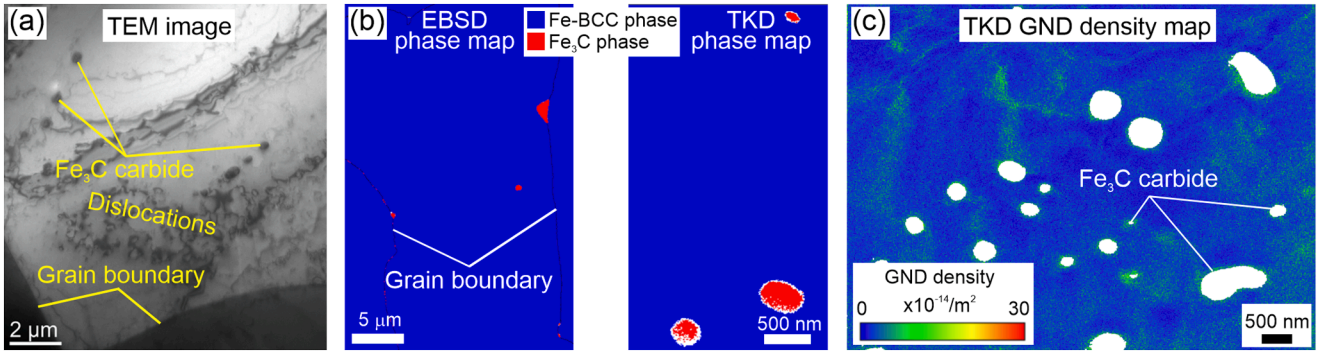

Fig. 4. Microstructure of the ferrite sample (top view direction): (a) TEM image showing carbides, grain boundaries, and dislocations, (b) EBSD (left side image) and TKD (right side image) phase maps showing different-sized Fe_3C carbides located at the grain boundaries and inside the grains, and (c) TKD GND density map showing density of generally necessary dislocations in the ferrite matrix.

3.2. Magnetic structure of ferrite and ferrite-pearlite

Microstructural and magnetic features determine the structure and properties of a ferromagnetic material. Besides the microstructure, the magnetic features are also influenced by external conditions such as applied or residual stresses [26]. However, here we did not separate possible internal stresses from the microstructures. To reveal the magnetic structure, both MFM (bulk sample, top view direction) and Lorentz microscopy (thin sample, top view direction) were used. Based on the MFM and Lorentz microscopy (Figs. 7–11), two different microstructures, ferrite and ferrite-pearlite, have differences also in the magnetic domain structure. Microstructural details such as the size, shape, and orientation of grain boundaries affect the distribution of DWs [6]. Generally, we noticed that the domain size in the ferritic-pearlitic structure is much smaller compared to the domain size in the plain ferritic structure. The topographic image (Fig. 7a) shows several ferrite grains in the bulk ferrite sample. The MFM image (Fig. 7a) shows that most of the grains in this scanned area have a maze-like pattern indicating that these grains are oriented close to the hard magnetization axis [1 1 1] of Fe-BCC agreeing with the EBSD results (Fig. 3a). The contrast in the MFM images is similar to the studies presented in [6,7] where the maze-like pattern predominates in the ferrite matrix. The topographic image (Fig. 7b) reveals several grains and globular and lamellar Fe_3C carbides in the bulk ferrite-pearlite sample. The MFM image (Fig. 7b) from the same area demonstrates the two-phase (Fe_3C and ferrite) magnetic contrast, which is typical for pearlite [5,6]. In the ferrite-

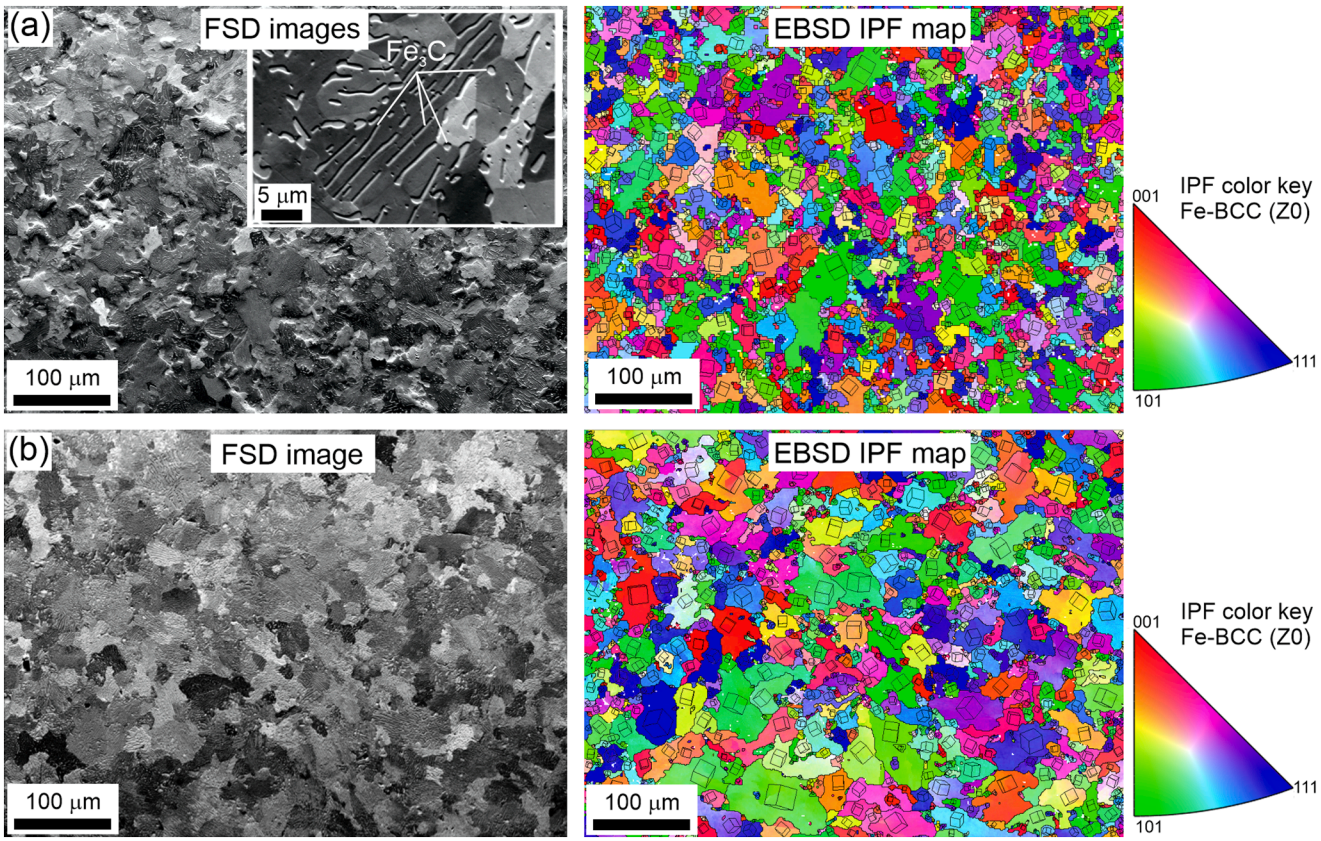

Fig. 5. Microstructure of the ferrite-pearlite sample: FSD image showing ferrite matrix with globular and lamellar Fe_3C carbides and EBSD IPF map to the normal direction (Z0) with grain boundaries (>10°) and unit cells showing orientation of ferrite grains. (a) Top view and (b) cross-section directions both showing similar microstructure with randomly oriented grains.

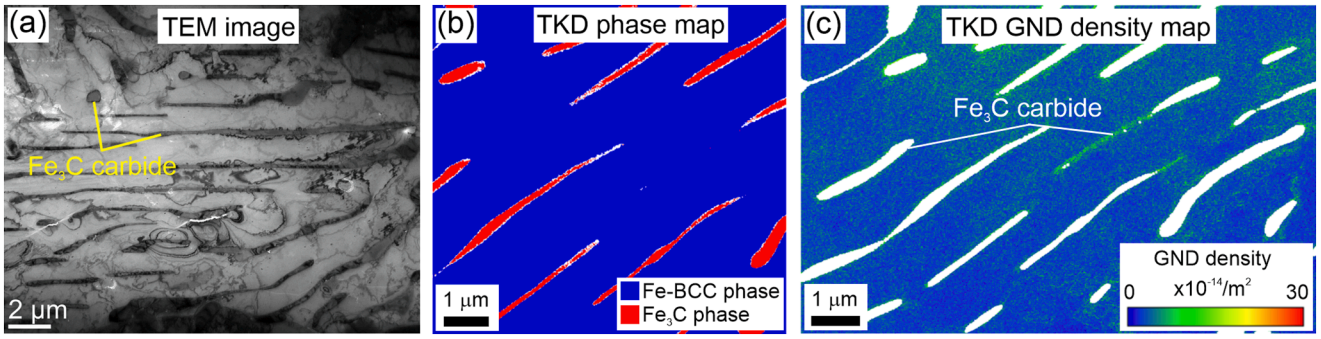

Fig. 6. Microstructure of the ferrite-pearlite sample (top view direction): (a) TEM image showing globular and lamellar Fe_3C carbides in the ferrite matrix, (b) TKD phase map showing Fe_3C carbides in the ferrite matrix, and (c) TKD GND density map showing density of generally necessary dislocations in the ferrite matrix.

pearlite sample, grains are randomly oriented (Fig. 5) and thus, MFM (Fig. 7b) is not showing as clear maze-like pattern as observed in the ferrite sample (Fig. 7a). The magnetic contrast in the Fe_3C carbides is discussed later.

One of our aims was to compare the magnetic structure in the bulk sample, studied by MFM, to the magnetic structure in the thin film studied by Lorentz microscopy. In Fig. 8, the topographic and MFM images collected from the bulk ferrite sample show a large grain located in the middle of the scanned area. This ferrite grain contains several magnetic domains with 90° and 180° DWs. A similar domain structure was observed with Lorentz microscopy with the thin sample. This highlights that similar details can be visualized with both methods from the bulk to thin sample.

Topographic, MFM, and Lorentz microscopy images collected from the ferrite-pearlite sample showing a region including mainly lamellar Fe_3C carbides are presented in Fig. 9. In both bulk and thin samples, DWs perpendicular and parallel to the lamellar Fe_3C carbides were observed. Some of the perpendicular DWs seem to intersect the carbides.

In Fig. 10, topographic and MFM images together with a Lorentz microscopy image show globular (Fig. 10a) and lamellar (Fig. 10b) Fe_3C carbides in the ferrite-pearlite sample. The DWs inside the globular and thicker lamellar carbides show very strong magnetic contrast in the MFM image whereas the ferrite matrix shows weaker contrast. The phase contrast in the MFM image arises from the differences in the magnetic properties of the ferrite matrix and Fe_3C carbides. The Fe_3C is magnetically harder than ferrite and thus causes stronger stray fields. The acquired MFM image is similar to those presented in [5,6]. According to both MFM and Lorentz microscopy, globular Fe_3C carbides

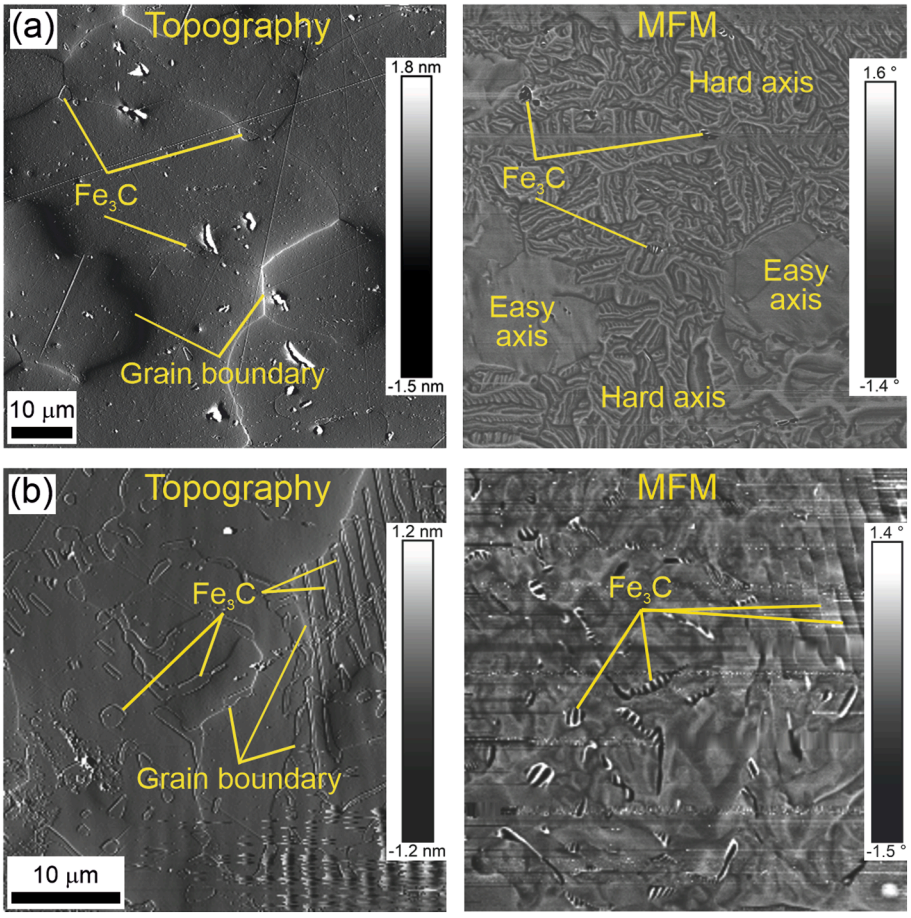

Fig. 7. Topographic and MFM images (bulk sample, top view direction) from (a) the ferrite sample showing several grains and that the hard magnetizing axis [1 1 1] dominates giving maze-like pattern to the MFM image and (b) the ferrite-pearlite sample showing grains and globular and lamellar Fe_3C carbides and weaker maze-like pattern in the MFM image compared to the ferrite sample because of almost missing grains orientated in the hard axis direction.

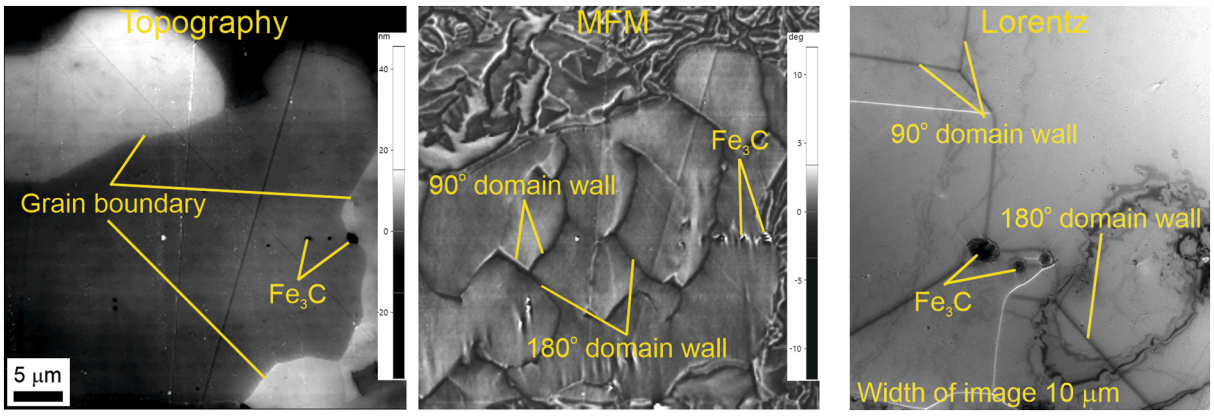

Fig. 8. Topographic and MFM images from the same ferrite sample area (bulk, top view direction) and Lorentz microscopy image from the ferrite sample (thin, top view direction) showing similar domain morphology in both bulk and thin samples.

(Fig. 10a) and thicker lamellar Fe_3C carbides (Fig. 10b) have their own, internal domain structure. In the thinner lamellae (Fig. 10b), no internal magnetic structure was observed, and they appear only as bright/dark lines in the MFM image (Fig. 7b).

We noticed that some of the observed magnetic features exist only in thin films such as the cross-tie domain walls. As we present in Fig. 11a, there are 'normal' DWs, i.e., white/black lines between the parallel Fe_3C lamellae and also cross-tie DWs, i.e., shorter white/black lines located perpendicular to the thin Fe_3C lamellae and vanishing at one end. We observed cross-tie DWs only by Lorentz microscopy in the thin sample as they are related to the thin film nature of the TEM samples. The cross-tie DWs have been described in [27–29]. Wiese *et al.* [30] observed them in NiFe (Permalloy) films with film thicknesses 30–70 nm. Recently, Kim and Park [10] observed cross-tie DWs by TEM in Z-type hexagonal ferrite thin film samples. By Lorentz microscopy, we observed arc-shaped domains next to some of the globular Fe_3C carbides (Fig. 11b). We did not observe this kind of DWs in the bulk samples.

To conclude, similar domain structure details were observed and

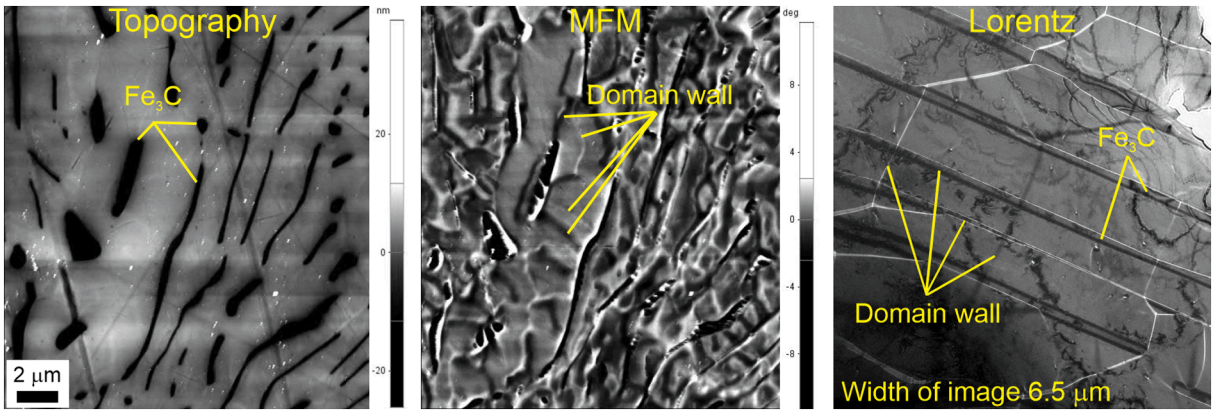

Fig. 9. Topographic and MFM images from the same ferrite-pearlite sample area (bulk, top view direction) and Lorentz microscopy image from the ferrite-pearlite sample (thin, top view direction) showing perpendicular and parallel domain walls to lamellar Fe_3C carbides in both bulk and thin samples.

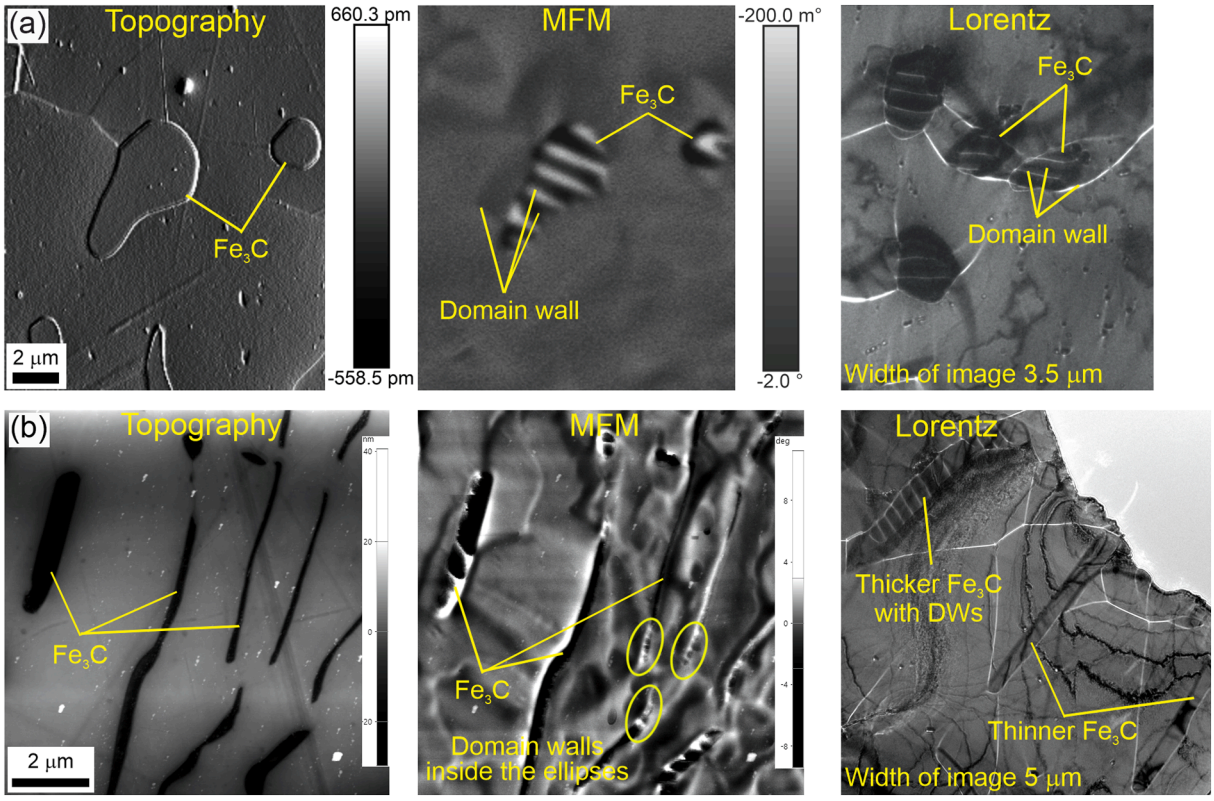

Fig. 10. Topographic and MFM images from the same ferrite-pearlite sample area (bulk, top view direction) and Lorentz microscopy image from the ferrite-pearlite sample (thin, top view direction). (a) Globular Fe_3C carbides showing their own domain structure and (b) lamellar Fe_3C carbides showing that only thicker lamellas have their own domain structure.

visualized in both bulk samples by MFM and thin films by Lorentz microscopy. Both methods, however, have their unique properties for contrast occurrence [27]. Lorentz microscopy provides only those DWs visible which are oriented optimally compared to the incident electron beam to yield net deflection of the electrons passing the thin sample. DWs that are most probably visible separate domains that are oriented perpendicularly towards the incident electron beam [27]. The same holds for the MFM as the phase shift is mainly proportional to the magnetic field gradient in vertical direction giving the best contrast from the strong stray field normal to the surface [6]. Therefore, in the actual BN measurements, the signal might also occur due to the motion of DWs that we cannot detect by Lorentz microscopy and/or MFM.

3.3. Origin of the domain wall movement

One of our aims was to move DWs and visualize their interaction with pinning sites by *in-situ* TEM, i.e., to visualize the origin of the BN signal. We observed that the crystal orientation of ferrite in the top view direction is dominantly of the type [1 1 1]. The observed domain wall movement with vertical external field is, however, not trivial, and thus we propose a possible mechanism for the movement here. We attribute the movement of the DWs on [1 1 1] surface to the interplay between the cubic magnetocrystalline anisotropy of the ferrite matrix and the external field induced vertical component of the magnetization. The easy axes of an Fe [1 1 1] surfaces are illustrated in Fig. 12a. The movement of the DW between two adjacent domains is generally driven

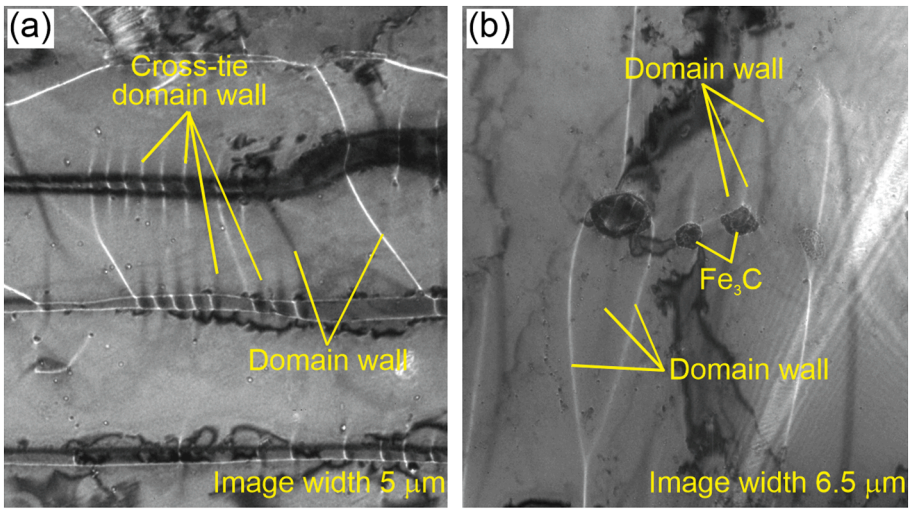

Fig. 11. Lorentz microscopy images showing (a) cross-tie domain walls in ferrite-pearlite and (b) arc-shaped domains next to globular Fe_3C carbides in ferrite.

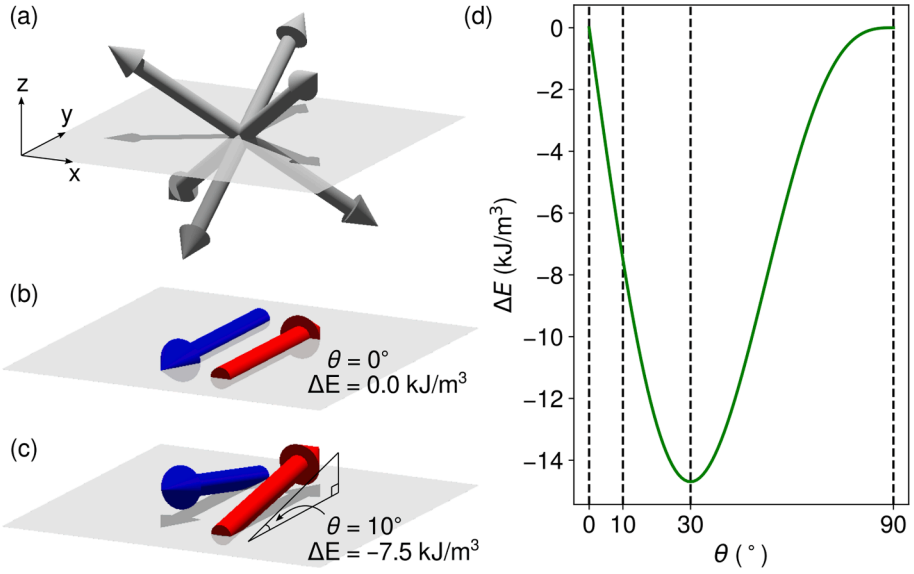

Fig. 12. Representation of magnetic anisotropy energetics on Fe[1 1 1] surface. (a) The cubic anisotropy easy axes. (b) The arrows represent the magnetization vectors of two different magnetic domains. The angle between the y- and z-components of the magnetization is $\theta = 0°$ for both domains. The anisotropy energy density difference between the domains is 0. The y-components of the magnetization are negative and positive for the blue and red arrows, respectively. (c) The angle between the y- and z-components of the magnetization is $\theta = 10°$ for both domains, resulting in the anisotropy energy density difference between the domains being 7.5 kJ/m^3. (d) Difference of the energy density between two domains for different angles θ, computed as $\Delta E = E(\mathbf{m}_{+y}) - E(\mathbf{m}_{-y})$ where $\mathbf{m}_{+y}$ and $\mathbf{m}_{-y}$ are magnetization vectors with positive and negative y-components, respectively. The energy densities are computed according to Equation (5). (For interpretation of the references to color in this figure legend, the reader is referred to the web version of this article.)

by the energy density difference of the two domains. In the following, we calculate the cubic anisotropy energy density for a given magnetization direction **m** (vector of unit length) using the traditional formula

$$E(\mathbf{m}) = K_{c1}[(\mathbf{m} \bullet \mathbf{c_1})^2(\mathbf{m} \bullet \mathbf{c_2})^2 + (\mathbf{m} \bullet \mathbf{c_1})^2(\mathbf{m} \bullet \mathbf{c_3})^2 + (\mathbf{m} \bullet \mathbf{c_2})^2(\mathbf{m} \bullet \mathbf{c_3})^2] \quad (5)$$

where K_{c1} is the first-order cubic anisotropy constant and $\mathbf{c_1}$, $\mathbf{c_2}$ and $\mathbf{c_3}$ are the anisotropy easy axes of unit length [26]. Modelling the ferrite matrix as Fe, we use the value of $K_{c1} = 48$ kJ/m^3 [26].

With domains of exactly in-plane magnetization on [1 1 1] surface, such as the configuration illustrated in Fig. 12b, all directions of magnetization are equally favorable in terms of the cubic anisotropy, and thus no movement of the DWs is expected. This configuration is typical on surfaces and in thin films, where the magnetic dipolar interactions tend to keep the magnetization in-plane or close to it with zero external field.

The applied vertical external field opposes the effect of the dipolar interaction and lifts the magnetic moment off the plane, as visualized in Fig. 12c, thus inducing a non-zero vertical component of the magnetization. The cubic anisotropy causes one of the domains to be more energetically favorable than the other, therefore making the DW movement a process that decreases the total energy of the system.

The difference of the energy densities of the different domains is shown in Fig. 12d as a function of the angle between the y- and z-components of the magnetization θ. We observe that between 0° and 30° the energy density difference is stronger with increased deviation of the magnetization from the plane, indicating that stronger vertical external field creates a stronger driving force on the DW while θ in this region. The energy density difference and the driving force are maximized at $\theta = 30°$, which is interestingly different from the angle between the surface and an easy axis that is 35.3°. Above 30°, increased external field suppresses the driving force. We note that the curve in Fig. 12d is calculated for a specific orientation of the domain wall with respect to the crystal orientation, so that the picture would change if the DW direction or the surface was rotated around the z-axis.

According to our examination, a similar mechanism does not exist for [1 0 0] and [1 1 0] surfaces. There, the possible domain wall movement is anticipated to occur due to thickness variation, dislocations, and other sources of residual stress in the sample; stress may induce local magnetic anisotropy, enabling the domain wall movement due to directional energetics in the same flavor as described above for [1 1 1] surfaces.

3.4. Visualization of interaction between domain walls and pinning sites

The effect of different microstructural details, i.e., pinning sites, on the DW motion in the ferrite sample is presented in Video 1 (the strength of the external magnetic field increases as a function of time, the width of the frame ~ 24.5 μm). In Fig. 13a, one frame of the Video 1 is presented showing different pinning sites such as dislocations, grain boundaries, and Fe_3C carbides as well as multiple DWs. According to Video 1, dislocations and grain boundaries have only a slight hindering effect on the DW motion when the strength of the external magnetic field increases, whereas carbides have a much stronger pinning effect. In our earlier study [15], we also noticed that the ferrite-ferrite grain boundary has no strong pinning effect. Video 1 presents as well the 90° DW mobility when the white DW is moving mainly with the motion of the 90° walls and the 180° wall in the middle of the frame changes its orientation perpendicularly in the increasing external magnetic field. In addition, expansion and contraction of domains occur.

Video 2 (the width of the first frame ~ 19 μm) shows the motion of DWs in the ferrite sample in the increasing external magnetic field: carbides seem to be very strong pinning sites while dislocations seem to bend DWs and exist as nucleation sites for new domains. This is also presented in Fig. 13b with still images (geometrically necessary dislocation density map collected by TKD superimposed to Lorentz microscopy image) from Video 2. It has been shown for nickel that dislocations themselves act both as the pinning centers for the motion of DWs and as the sites for domain nucleation [31]. In the increasing external magnetic field, the interaction of a moving DW with the Fe_3C carbides in the ferrite sample is presented with higher magnification in Video 3 (the width of the frame ~ 7.5 μm). In the plain ferritic structure, the Fe_3C carbides act as strong pinning sites for DW motion. The assumption for Fe_3C carbides is that they are considered to behave as strong pinning barriers to the DW motion [32]. However, with increased magnetic field strength, the domain wall can pass the carbides. According to the TKD results (Fig. 5c), dislocations seem to surround the carbides agreeing with the results presented by Batista *et al.* [6].

The interaction of DWs in the more complicated microstructure of the ferrite-pearlite sample with both globular and lamellar Fe_3C carbides is presented in Video 4 (the strength of the external magnetic field increases as a function of time; the width of the frame is ~ 15 μm). Fig. 9 illustrates the DWs that are oriented either parallel or perpendicular to the lamellar Fe_3C carbides. This kind of DWs exist also in Video 4, comprising three different time periods from a single experiment; time frames between the periods are removed where no changes occur. Video 4 shows that movements of the DWs parallel to the Fe_3C lamellae are minimal compared to the notable motions of the DWs perpendicular to the lamellae. Lo *et al.* [33] and Hetherington *et al.* [34] found that Fe_3C lamellae parallel to the DWs were stronger pinning sites than lamellae perpendicular to the DWs. Altpeter [17] explained that as the cementite volume is increased in the structure together with the residual stress decreasing due to the equilibrium of the stress state, the tensile stresses increase in the ferrite phase which increasingly hinders the 90° DW motion in the matrix. According to the theoretical considerations by Laszlo [35], differences in the cementite shape (either being globular or lamellar) and size cause different residual stress fields; lamellar Fe_3C carbides having a stronger pinning effect than globular carbides.

Fe_3C carbides are known to have their own domain structure that reduces the magnetostatic energy of the system [35]. Altpeter [17] speculated that the DWs in the ferrite matrix interact with the DWs in cementite. As presented in Fig. 10, the Fe_3C carbides have their own magnetic structure. Video 5 (the strength of the external magnetic field

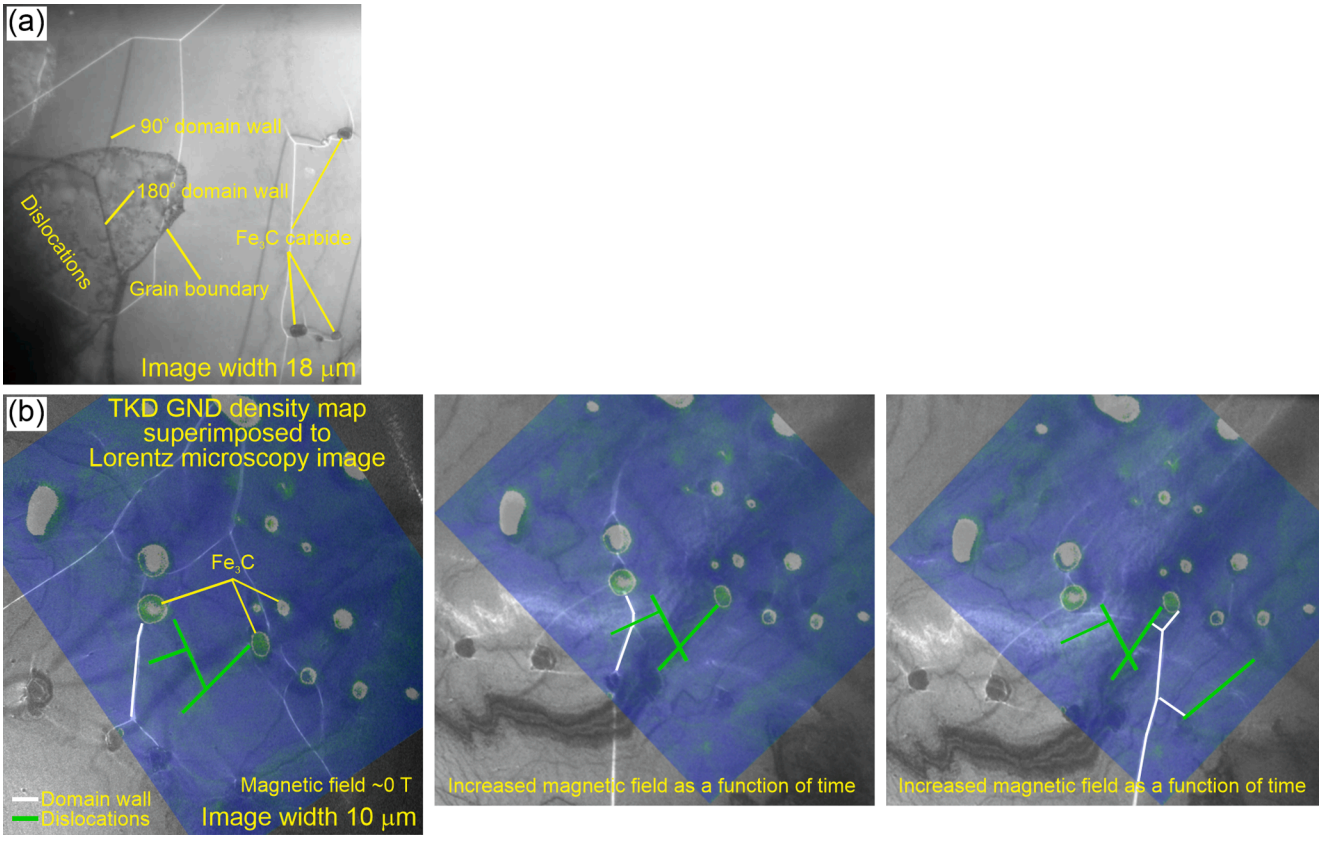

Fig. 13. (a) A frame (Lorentz microscopy) from Video 1 showing various pinning sites: carbides, dislocations, and grain boundaries. (b) Geometrically necessary dislocation density maps collected by TKD superimposed to Lorentz microscopy images (frames from the Video 2) showing the motion of domain walls in the increasing external magnetic field: carbides seem to be very strong pinning sites while dislocations seem to bend domain walls and exist as nucleation sites for new domain walls.

increases as a function of time, the width of the frame ~ 8 μm) reveals that only slight changes of DWs inside the Fe_3C carbides can be observed even though the magnetic field strength is increased to similar values where notable changes occur in the ferrite matrix. It is questionable if these minor magnetic changes inside Fe_3C carbides produce any BN signal. We did not observe interactions between DWs in the ferrite matrix and DWs in the cementite carbides. Batista *et al.* [6] stated that the magnetic moments in the Fe_3C carbides are not easily oriented by the applied magnetic field due to the very high anisotropy of the carbides. Altpeter [17] noticed that, during the magnetization process of soft iron, the low density of dislocations and lattice defects will involve the 90° DWs motion. The 90° DWs are said to be stress-sensitive in contrast to the 180° DWs [36], and the 90° DWs have a strong interaction with the cementite carbides and thus their motion is hindered. We observe and show this in Video 1, where at 00:24 s, the moving 90° DW is pinned by the Fe_3C carbides for some time before it continues to move in the increasing magnetic field.

3.5. Analysis of Barkhausen noise measurements combined to microscopy techniques

The BN measurements were carried out for the bulk SEM samples (top view and cross-section directions) and for pre-thinned TEM samples with the same BN equipment and measurement parameters. In the case of the top view direction of the bulk ferrite sample, the BN measurements were carried out by applying the magnetic field in two different directions: rolling direction (RD) and transverse to the rolling direction (TD). As many different procedures will influence the BN outcome, the interpretation of the results is not straightforward. In this study, ferritic and ferrite-pearlitic microstructures were not processed from the same steel composition. Therefore, there might be differences in the BN outcome, for example due to the different carbon contents of the samples as presented in [37]. The higher carbon content increases the number of pinning sites (as carbides are formed) that prevent the free movement of the DWs. Further, it increases the BN signal amplitude as much higher magnetic field is needed to overcome the pinning sites [37].

The bulk ferrite sample (top view) gave a higher RMS value compared to the ferrite-pearlite (top view) sample (Table 2). The rolling produced the texture for the ferrite sample as shown in Fig. 3. In the presence of the texture, the BN is said to become dependent on the orientation of the grains as well [32]. Therefore, as Abuthahir and Kumar [7] stated, the crystallographic texture, apart from the pinning sites, determines the energy required for the magnetization of the material. In our studies, the BN measurements of the bulk ferrite sample (top view) to RD had slightly higher RMS value than the measurements to TD (Table 2). Both directions, RD and TD, had a high number of grains to the hard axis direction but the grain morphology (texture) was different (Fig. 3a). In this case, the amount of grain boundaries is higher to the TD (flattened grains) than to the RD (longitudinal grains). As the measurement in the RD leads to DW movement in the TD, the higher RMS value of the BN signal in the RD is consistent with the higher amount of grain boundaries in the direction of the DW movement.

Table 2
Direct Barkhausen noise results from Microscan for ferrite and ferrite-pearlite samples (1.5 vpp, 300 Hz).

	RMS average	Pulse count
Bulk ferrite RD (top view)	169	4445
Bulk ferrite TD (top view)	139	4512
Bulk ferrite (cross-section)	147	4445
Thin (0.10 mm) ferrite (top view)	222	4511
Thin (0.07 mm) ferrite (top view)	405	4646
Bulk ferrite-pearlite (top view)	124	4933
Bulk ferrite-pearlite (cross-section)	159	4849
Thin (0.11 mm) ferrite-pearlite (top view)	257	4937
Thin (0.06 mm) ferrite-pearlite (top view)	434	4939

To compare the possible orientation influence on the BN signal, the ferrite bulk sample was measured from top view (RD, TD) and cross-section directions. The BN envelopes for these are presented in Fig. 14a. As mentioned earlier, the BN pick-up measurement direction is normal to the surface [25]. In the top view of the ferrite bulk sample, the hard magnetic axis [1 1 1] is favored (Fig. 3a). As stated in [38], the produced magnetization curve is dependent on the orientation of the magnetic field (H) relative to the easy axes. Jiles [38] observed the response of magnetic induction (B) or magnetization (M) as a function of H to increase steeper to the direction of the easy axis [1 0 0] than to the hard axis [1 1 1]. Therefore, the hard axis direction acts as a stronger barrier for the magnetic reversal and causes lower RMS. Also, contradictory claims exist as Ortega-Labra *et al.* [25] stated that the magnetocrystalline anisotropy mainly influences the domain nucleation and annihilation processes. Our ferrite bulk sample, as measured in the cross-section direction, yielded lower RMS value (Table 2) compared to the top view RD which does not follow the similar trend as presented in [38]. The envelopes (Fig. 14a) of the ferrite bulk top view (RD, TD) and cross-section and the ferrite-pearlite bulk and cross-section (Fig. 14b) correspond well to the RMS averages in Table 2.

The RMS value of the ferrite-pearlite bulk sample measured in the top view direction is smaller than in the cross-section direction (Table 2). The envelopes for these are presented in Fig. 14b which shows that the BN signal starts earlier for cross-section sample and has higher amplitude compared to the bulk (top view). The OM images taken from these directions (Fig. 15) show that the density of Fe_3C carbides is much higher in the cross-section direction than in the top view direction. This produces different magnetic domain structure and density of pinning sites which probably explain the difference in the RMS values and different BN envelope features. According to Clapham *et al.* [32], the preferred orientation relationships between adjacent pearlite colonies may influence the BN signal production by allowing long mean free paths for moving DWs and giving thus large BN pulses, i.e., higher RMS. To conclude, for ferrite with rolled structure, the change in the RMS average is more drastic when comparing the RD and TD measurement directions than the measurements taken from the top view and cross-section directions.

Two different thicknesses of pre-thinned TEM sheets were measured from both materials. The pulse count values were similar for bulk and pre-thinned samples (Table 2). The pre-thinned samples had higher RMS values compared to the bulk samples (Table 2), but the RMS value depended much on the thickness of the thin sample; thinner ferrite (0.07 mm) and ferrite-pearlite (0.06 mm) gained higher RMS values than thicker ones (0.10 – 0.11 mm). The increase in the RMS values was more profound in the case of the thin ferrite-pearlite sample compared to the bulk samples. We attribute the variation of RMS values to the skin depth of the driving field. Due to the shape anisotropy, the magnetization reversal process has restrictions close to the surfaces of the sample, so that the reversal process via the vertical direction has a relatively high energy barrier [39,40]. Consequently, the pinning of the DWs is enhanced, and the resulting BN becomes stronger in comparison to the bulk part, where weaker BN occurs due to more rotational degrees of freedom of the magnetic moments. The thicknesses of our thin samples are of the same order of magnitude as the skin depth, and therefore the distance of the measurement device to the *bottom* surface of the sample is relevant in terms of the BN signal. Loosely speaking, the observed BN signals of the thinnest samples result from the contribution of both surfaces (top and bottom). In thicker samples, the driving field is weaker at the bottom surface, and the BN signal is consequently weaker. In thick samples (where thickness clearly exceeds the skin depth), another mechanism contributing to weaker BN signals might occur: Parts of long domain walls far away from the surface, that do not experience the driving field, are being dragged along by the parts of the domain walls closer to the surface that are driven by the external field. This leads to suppressed overall mobility of the DWs and decreased BN signal.

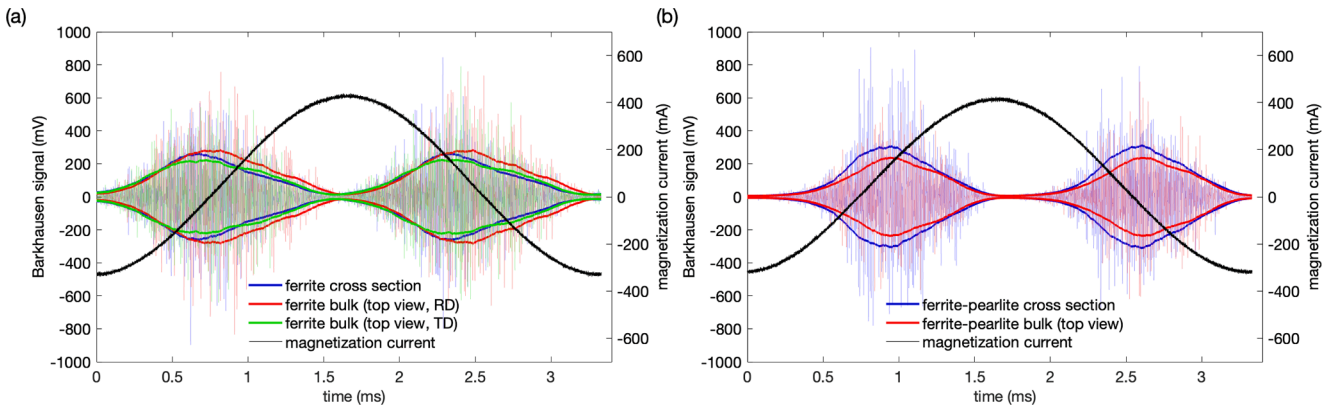

Fig. 14. Representation of Barkhausen noise envelopes (colored curves, left axes) together with the magnetization current (black curves show the current for the bulk samples, right axes) of (a) ferrite bulk (top view, RD and TD) and cross-section samples and (b) ferrite-pearlite bulk top view and cross section samples. The thick lines show RMS envelopes computed with a window size of 0.156 ms and averaged over several BN bursts, while the thin, partially transparent lines show examples of BN signals of individual bursts.

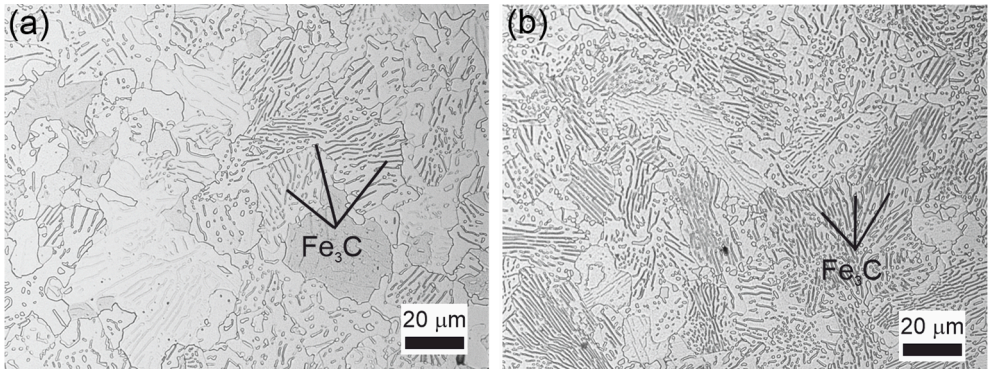

Fig. 15. Optical microscope images of the bulk ferrite-pearlite sample (etched by 4 % Nital), (a) top view direction and (b) cross-section direction showing higher density of Fe_3C carbides in the cross-section direction than in the top view direction.

The Lorentz microscopy is carried out at locations of the thin samples where the thickness is decreased to<100 nm by electropolishing. With such thicknesses, the contribution from the bulk material to the DW dynamics is minimal and the surface effects dominate the magnetic behavior. In general, Barkhausen noise from thin films below 100 nm in thickness is not well understood mostly due to the challenges in measuring the weak BN signal from such thin samples. To our knowledge, the effect of the film thickness has only been studied in terms of the critical exponents of the Barkhausen jump size distributions [41], and no thickness dependence on the exponents has been observed. In our samples, however, the thinnest, polished area of the sample (electron transparent area, thickness < 100 nm) is small compared to the BN sensor size, and thus the measured BN signal is not expected to contain essential contribution from the thin, polished area. Based on Lorentz microscopy, ferrite-pearlite has a significantly higher amount of cross-tie domain walls compared to ferrite. According to the *in-situ* TEM studies, cross-tie DWs moved together with 'parent' DWs in the increasing magnetic field.

The BN envelopes for ferrite and ferrite-pearlite samples are presented in Fig. 16 separately for each microstructure with bulk samples

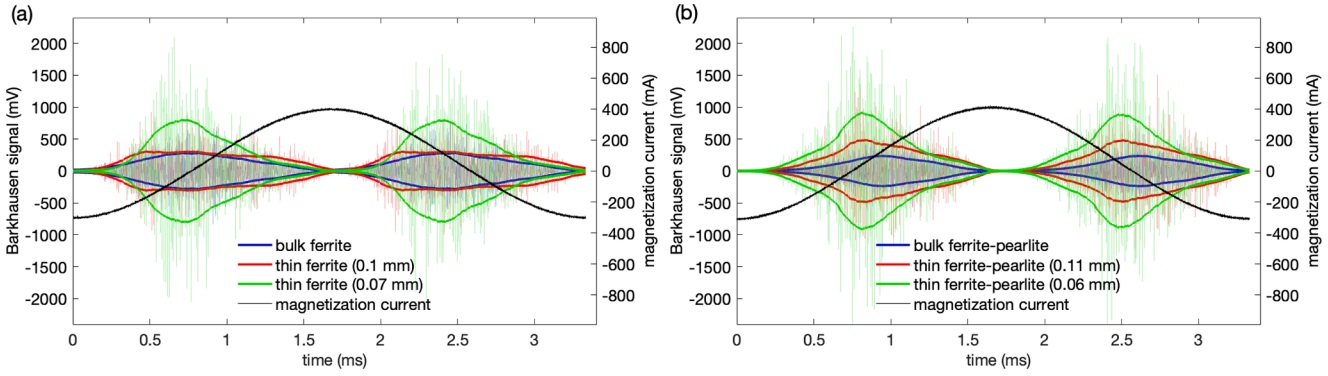

Fig. 16. Representation of Barkhausen noise envelopes (colored curves, left axes) together with the magnetization current (black curves show the current for the bulk samples, right axes) of (a) ferrite and (b) ferrite-pearlite bulk samples (RD) and pre-thinned sheets. The thick lines show RMS envelopes computed with a window size of 0.156 ms and averaged over several BN bursts, while the thin, partially transparent lines show examples of BN signals of individual bursts.

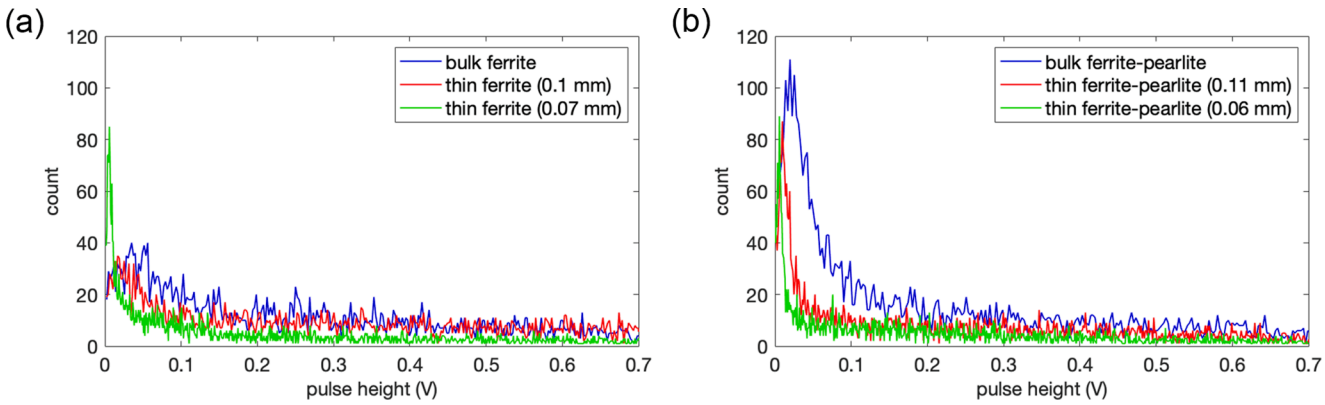

Fig. 17. Pulse height distributions for (a) ferrite and (b) ferrite-pearlite bulk samples and pre-thinned sheets expressed up to 0.7 V.

and pre-thinned TEM sheets with two thicknesses. The thinnest (0.06 mm) ferrite-pearlite sheet has a larger envelope compared to the ferrite-pearlite bulk sample and the other thin sheet (0.11 mm). This was observed also for ferrite samples. In both bulk and thin sheets of ferrite-pearlite, the pulse count is higher compared to the ferrite samples and sheets (Table 2). This is due to a higher amount of pinning sites in the ferrite-pearlite than in the plain ferritic structure. Similar result is expressed in [38].

Among other features, the DW motion is influenced by the density of the obstacles and the different pinning strengths of certain types of obstacles. As Fig. 17 shows, together with the information of pulse counts (Table 2) and the microscopy observations (e.g., Figs. 9 and 10), the ferritic-pearlitic structure has more hindrances to the DW motion compared to the plain ferritic structure. Thus, it creates a higher number of individual BN events, observed as higher pulse count value, for bulk and thin (0.11 mm) ferrite-pearlite. However, they have a smaller amplitude (<0.05 V) compared to the ferritic structure (Fig. 17a). Similar behavior is presented in [42]. Accordingly, in ferrite, with a smaller number of hindrances, the smaller number of BN events (pulse count values, Table 2) was observed compared to ferrite-pearlite. These findings are in good correlation with our microstructural studies of the samples. Based on Video 4 collected from the ferrite-pearlite sample, several small DW displacements were noticed but long DW jumps were not observed. For the thinnest ferrite sheet, a high amount of very small pulses is observed (Fig. 17a) and the corresponding increase is found in the pulse counts (Table 2) compared to other measured ferrite samples. It should be noticed that all DWs may not be visible in Lorentz microscopy due to the contrast formation and therefore all DW motion might not be seen which, however, will affect the BN signal.

4. Conclusions

We characterized the ferrite and ferrite-pearlite samples thoroughly by SEM-EBSD, SEM-TKD, MFM, and *in-situ* TEM together with Lorentz mode to get fundamental information about pinning sites of the DW motion and especially their interaction with DWs. Characterization results were utilized to make the connection between microstructural features and BN outputs. Some of these characterization techniques require a thin sample (TKD and Lorentz microscopy), whereas industrial BN measurements are typically carried out for bulk samples. Thus, we used MFM to compare and combine results of thin and bulk samples. This comparison was very important because we used *in-situ* TEM (thin sample) to visualize the motion of DWs and we connected these findings to BN signals (bulk sample). It can be concluded that:

- Earlier studies have presented various hypotheses about the origin of Barkhausen noise. Here, we visualize and testify many hypotheses by means of SEM-EBSD-TKD, MFM, and *in-situ* TEM together with Lorentz microscopy.
- Our thorough characterization enabled us to resolve the origin of the varying BN signal levels in plain ferrite with several features (e.g., texture due to rolling and hard/easy axis orientation), theoretically affecting the BN output.
- Interaction of DWs and pinning sites, i.e., origin of Barkhausen noise, in ferrite-pearlite with globular and thin and thick lamellar Fe_3C carbides was revealed with our multi-instrumental analysis: larger globular and thicker lamellar carbides have their own magnetic structure and DWs parallel and perpendicular to lamellas exist in the ferrite matrix. Carbides are strong pinning sites and DWs parallel to the lamella need a strong applied magnetic field to move.
- We indicated that bulk and thin samples have similar magnetic structure nevertheless giving different BN signal. The thickness of the thin sample is similar to the magnitude of the skin depth. Thus, the observed BN signals of the thinnest samples result from the contribution of both surfaces (top and bottom). In thicker samples, the driving field is weaker at the bottom surface, and the BN signal is consequently weaker.
- We showed that the thickness of the sample affects the RMS value of Barkhausen noise: The pre-thinned samples had higher RMS values compared to the bulk samples. The observed BN signals of the thinnest samples result from the contribution of both surfaces (top and bottom). In thick samples, parts of long DWs far away from the surface are being dragged along by the parts of the DWs closer to the surface that are driven by the external field. This leads to suppressed overall mobility of the DWs and decreased BN signal.
- We could explain an in-plane DW movement under out-of-plane applied magnetic field (*in-situ* TEM) using anisotropy energetics.
- BN results correlate well with the DW movements visualized by *in-situ* TEM. To help the interpretation of DW motions, alignment and denoising processes were tailored for the frames collected during *in-situ* TEM studies.
- In the future, the combination of correlative microscopy and micromagnetic simulations will provide more quantitative analysis of the origin of the Barkhausen noise by offering deep, physics-based understanding of the interaction between domain walls and material imperfections.

Declaration of Competing Interest

The authors declare that they have no known competing financial interests or personal relationships that could have appeared to influence the work reported in this paper.

Data availability

Data will be made available on request.

Acknowledgements

This work was supported by Research Council of Finland [grant numbers 338954, 338955]. Microscopy work made use of Tampere Microscopy Center facilities at Tampere University. We would like to thank B.Sc. Justus Rantala for assistance in the sample preparation.

Appendix A. Supplementary data

Supplementary data to this article can be found online at https://doi.org/10.1016/j.matdes.2023.112308.

References:

[1] A. Ktena, E. Hristoforou, G.J.L. Gerhardt, F.P. Missell, F.J.G. Landgraf, D. L. Rodrigues, M. Alberteris-Campos, Barkhausen noise as a microstructure characterization tool, Phys. B Condens. Matter 435 (2014) 109–112, https://doi.org/10.1016/j.physb.2013.09.027.
[2] J. Liu, G.Y. Tian, B. Gao, K. Zeng, Y. Zheng, J. Chen, Micro-macro characteristics between domain wall motion and magnetic Barkhausen noise under tensile stress, J. Magn. Magn. Mater. 493 (2020), 165719, https://doi.org/10.1016/j.jmmm.2019.165719.
[3] I. Manke, N. Kardjilov, R. Schäfer, A. Hilger, M. Strobl, M. Dawson, C. Grünzweig, G. Behr, M. Hentschel, C. David, A. Kupsch, A. Lange, J. Banhart, Three-dimensional imaging of magnetic domains, Nat. Commun. 1 (2010) 125, https://doi.org/10.1038/ncomms1125.
[4] M.R. Freeman, B.C. Choi, Advances in magnetic microscopy, Science 294 (2001) 1484–1488, https://doi.org/10.1126/science.1065300.
[5] J.T. Thornton, Metal surface investigation by scanning probe microscopy, Surf. Eng. 16 (2000) 287–293, https://doi.org/10.1179/026708400101517224.
[6] L. Batista, U. Rabe, I. Altpeter, S. Hirsekorn, G. Dobmann, On the mechanism of nondestructive evaluation of cementite content in steels using a combination of magnetic Barkhausen noise and magnetic force microscopy techniques, J. Magn. Magn. Mater. 354 (2014) 248–256, https://doi.org/10.1016/j.jmmm.2013.11.019.
[7] J. Abuthahir, A. Kumar, Magnetic force microscopy studies in bulk polycrystalline iron, J. Magn. Magn. Mater. 448 (2018) 107–116, https://doi.org/10.1016/j.jmmm.2017.06.107.
[8] I. Manke, N. Kardjilov, R. Schäfer, A. Hilger, R. Grothausmann, M. Strobl, M. Dawson, C.h. Grünzweig, C.h. Tötzke, C.h. David, A. Kupsch, A. Lange, M. P. Hentschel, J. Banhart, Three-dimensional imaging of magnetic domains with neutron grating interferometry, Phys. Procedia 69 (2015) 404–412, https://doi.org/10.1016/j.phpro.2015.07.057.
[9] M. Di Pietro Martínez, A. Wartelle, C. Herrero Martínez, F. Fettar, F. Blondelle, J.-F. Motte, C. Donnelly, L. Turnbull, F. Ogrin, G. van der Laan, H. Popescu, N. Jaouen, F. Yakhou-Harris, G. Beutier, Three-dimensional tomographic imaging of the magnetization vector field using Fourier transform holography, Phys. Rev. B 107 (2023), 094425, https://doi.org/10.1103/PhysRevB.107.094425.
[10] S.-D. Kim, I. Park, Real-time observation of magnetic domain structure changes with increasing temperature for Z-type hexagonal ferrite, Materials. 15 (2022) 3646, https://doi.org/10.3390/ma15103646.
[11] T. Ickler, H. Meckbach, F. Zeismann, A. Brückner-Foit, Assessing the influence of crystallographic orientation, stress and local deformation on magnetic domains using electron backscatter diffraction and forescatter electron imaging, Ultramicroscopy 198 (2019) 33–42, https://doi.org/10.1016/j.ultramic.2018.12.012.
[12] S. Santa-aho, A. Laitinen, A. Sorsa, M. Vippola, Barkhausen noise probes and modelling: a review, J. Nondestr. Eval. 38 (2019) 94, https://doi.org/10.1007/s10921-019-0636-z.
[13] S. Santa-aho, A. Sorsa, M. Ruusunen, M. Vippola, Grinding burn classification with surface Barkhausen noise measurements, E-Journal of Nondestructive Testing. 1 (1) (2023).
[14] S. Santa-aho, A. Sorsa, M. Honkanen, M. Vippola, Detailed Barkhausen noise and microscopy characterization of Jominy end-quench test sample of CF53 steel, J. Mater. Sci. 55 (2020) 4896–4909, https://doi.org/10.1007/s10853-019-04284-z.
[15] M. Honkanen, S. Santa-aho, L. Laurson, N. Eslahi, A. Foi, M. Vippola, Mimicking Barkhausen noise measurement by in-situ transmission electron microscopy - effect of microstructural steel features on Barkhausen noise, Acta Mater. 221 (2021), 117378, https://doi.org/10.1016/j.actamat.2021.117378.
[16] H. Sheng, P. Wang, C. Tang, Y. Shi, Y. Zheng, Microstructure and mechanical properties evaluation of automotive plate steel based on micromagnetic NDT technologies, Measurement 199 (2022), 111459, https://doi.org/10.1016/j.measurement.2022.111459.
[17] I. Altpeter, Nondestructive evaluation of cementite content in steel and white cast iron using inductive Barkhausen noise, J. Nondestr. Eval. 15 (1996) 45–60, https://doi.org/10.1007/BF00729134.
[18] Oxford Instruments, Electron Backscatter Diffraction, (2023). www.ebsd.com.
[19] N. Eslahi, A. Foi, Joint Sparse Recovery of Misaligned Multimodal Images via Adaptive Local and Nonlocal Cross-Modal Regularization, in: 2019 IEEE 8th International Workshop on Computational Advances in Multi-Sensor Adaptive Processing (CAMSAP), 2019: pp. 111–115. https://doi.org/10.1109/CAMSAP45676.2019.9022478.
[20] L. Azzari, L.R. Borges, A. Foi, Modeling and Estimation of Signal-Dependent and Correlated Noise, in: M. Bertalmío (Ed.), Denoising of Photographic Images and Video: Fundamentals, Open Challenges and New Trends, Springer International Publishing, Cham, 2018, pp. 1–36, https://doi.org/10.1007/978-3-319-96029-6_1.
[21] G.K. Froehlich, J.F. Walkup, R.B. Asher, Optimal estimation in signal-dependent noise, J. Opt. Soc. Am., JOSA. 68 (1978) 1665–1672, https://doi.org/10.1364/JOSA.68.001665.
[22] E. Mäntylä, T. Montonen, L. Azzari, S. Mattola, M. Hannula, M. Vihinen-Ranta, J. Hyttinen, M. Vippola, A. Foi, S. Nymark, T.O. Ihalainen, Iterative immunostaining combined with expansion microscopy and image processing reveals nanoscopic network organization of nuclear lamina, (2023) 2022.09.27.509734. https://doi.org/10.1101/2022.09.27.509734.
[23] M. Maggioni, E. Sánchez-Monge, A. Foi, Joint removal of random and fixed-pattern noise through spatiotemporal video filtering, IEEE Trans. Image Process. 23 (2014) 4282–4296, https://doi.org/10.1109/TIP.2014.2345261.
[24] Thomas, J, Fix, R.M., Optimizing Magnetization Parameters of Magnetic Barkhausen Noise for More Accurate Detection of Residual Stresses and Variations in Microstructure, in: Proceedings of the 7th International Conference on Barkhausen Noise and Micromagnetic Testing (ICBM 7), 2009.
[25] O. Ortega-Labra, P. Martínez-Ortiz, T.L. Manh, E. Velazquez-Lozada, J.A. Perez-Benitez, What does a Barkhausen surface coil actually measure? J. Magn. Magn. Mater. 563 (2022), 169938 https://doi.org/10.1016/j.jmmm.2022.169938.
[26] B.D. Cullity, C.D. Graham, Introduction to magnetic materials, 2nd ed, IEEE/Wiley, Hoboken, N.J., 2009.
[27] A. Hubert, R. Schäfer, Magnetic Domains: The Analysis of Magnetic Microstructures, Springer Science & Business Media, 1998.
[28] K.L. Metlov Institute of Physics ASCR, Na Slovance 2, Prague 8, 18221, Czech Republic Simple analytical description for the cross-tie domain wall structure Applied Physics Letters. 79 16 2001 2001 2609 2611.
[29] K.L. Metlov, Cross-tie domain wall ground state in thin films, J. Low Temp. Phys. 139 (2005) 207–219, https://doi.org/10.1007/s10909-005-3924-1.
[30] N. Wiese, S. McVitie, J.N. Chapman, A. Capella-Kort, F. Otto, On the scaling behaviour of cross-tie domain wall structures in patterned NiFe elements, EPL 80 (2007) 57003, https://doi.org/10.1209/0295-5075/80/57003.
[31] Z. Xiang, Q. Sun, S. Wang, Effect of dislocation pattern on the magnetic domain structure of pure polycrystalline Ni, J. Mater. Res. Technol. 17 (2022) 1896–1900, https://doi.org/10.1016/j.jmrt.2022.01.107.
[32] L. Clapham, C. Jagadish, D.L. Atherton, The influence of pearlite on Barkhausen noise generation in plain carbon steels, Acta Metall. Mater. 39 (1991) 1555–1562, https://doi.org/10.1016/0956-7151(91)90242-S.
[33] C.C.H. Lo, C.B. Scruby, G.D.W. Smith, Dependences of magnetic Barkhausen emission and magnetoacoustic emission on the microstructure of pearlitic steel, Phil. Mag. 84 (2004) 1821–1839, https://doi.org/10.1080/14786430410001663196.
[34] M.G. Hetherington, J.P. Jakubovics, J.A. Szpunar, B.K. Tanner, High-voltage Lorentz electron microscopy studies of domain structures and magnetization processes in pearlitic steels, Philos. Mag. B 56 (1987) 561–577, https://doi.org/10.1080/13642818708220163.
[35] F. Laszlo, Tessellated Stresses - Part I, J. Iron Steel Inst. 147 (1943) 173–199.
[36] D. Jiles, Introduction to magnetism and magnetic materials, in: Chapman and Hall, New York, 1991: p. 440.
[37] T.u. Le Manh J.A. Pérez Benitez J.H. Espina Hernández J.M. Hallen López Barkhausen Noise for Non-Destructive Testing and Materials Characterization in Low Carbon Steels 2020 Elsevier 95 114.
[38] D.C. Jiles, Dynamics of domain magnetization and the Barkhausen effect, Czech J. Phys. 50 (2000) 893–924, https://doi.org/10.1023/A:1022846128461.
[39] G. Durin, S. Zapperi, The Barkhausen effect, (2004). https://doi.org/10.48550/arXiv.cond-mat/0404512.
[40] L. Néel, Energie des parois de Bloch dans les couches minces, Comptes Rendus Hebdomadaires Des Seances De L Academie Des Sciences. 241 (1955) 533.
[41] L. Santi, F. Bohn, A.D.C. Viegas, G. Durin, A. Magni, R. Bonin, S. Zapperi, R. L. Sommer, Effects of thickness on the statistical properties of the Barkhausen noise in amorphous films, Phys. B Condens. Matter 384 (2006) 144–146, https://doi.org/10.1016/j.physb.2006.05.176.
[42] O. Saquet, J. Chicois, A. Vincent, Barkhausen noise from plain carbon steels: analysis of the influence of microstructure, Mater. Sci. Eng. A 269 (1999) 73–82, https://doi.org/10.1016/S0921-5093(99)00155-0.